MULTI-JAM SOLUTIONS IN TRAFFIC MODELS WITH VELOCITY-DEPENDENT DRIVER STRATEGIES

PAUL CARTER*, PETER LETH CHRISTIANSEN†, YURI B. GAIDIDEI‡, CARLOS GORRIA§, BJÖRN SANDSTEDE¶, MADS PETER SØRENSEN‖, AND JENS STARKE‖

Abstract. The optimal-velocity follow-the-leader model is augmented with an equation that allows each driver to adjust their target headway according to the velocity difference between the driver and the car in front. In this more detailed model, which is investigated on a ring, stable and unstable multi-pulse or multi-jam solutions emerge. Analytical investigations using truncated Fourier analysis are confirmed and complemented by a detailed numerical bifurcation analysis. In addition to standard rotating waves, time-modulated waves are found.

1. Introduction. Understanding vehicular traffic flow, and in particular the formation of traffic jams, is a major undertaking that can benefit from mathematical modeling. Indeed, mathematical modeling of traffic flow has a long history, and we refer, for instance, to [5, 15, 18, 28] for comprehensive reviews. The most commonly used models can be divided into two groups. Microscopic models attempt to model individual cars through differential equations (one example is the optimal-velocity model [3] that will be described below) or cellular automata (such as the Nagel-Schreckenberg model [19]) that adjust the velocity of individual cars based on the position and velocity of the preceding car or cars. Macroscopic models are based on continuum approximations of the density of cars: these models involve partial differential equations (PDEs) for density and velocity. Macroscopic models can arise as appropriate limits of microscopic models; see, e.g., [1, 14] for typical examples of such results.

Common features of microscopic and macroscopic models are free-flow solutions, where cars are equally spaced and move uniformly with identical speed, and traveling-wave solutions that correspond to traffic jams. Many works have focused on the existence, stability, and bifurcations of these solutions, and we refer to [3] and [6, 12] for a few selected investigations of microscopic and macroscopic models, respectively.

*Department of Mathematics, Brown University, Providence, RI 02912, USA

†Department of Applied Mathematics and Computer Science & Department of Physics, Technical University of Denmark, DK-2800 Kongens Lyngby, Denmark

‡Bogolyubov Institute for Theoretical Physics, Metrologichna str. 14 B, 03680, Kiev, Ukraine

§Department of Applied Mathematics and Statistics, University of the Basque Country, E-48080 Bilbao, Spain

¶Division of Applied Mathematics, Brown University, Providence, RI 02912, USA

‖Department of Applied Mathematics and Computer Science, Technical University of Denmark, DK-2800 Kongens Lyngby, Denmark

Generally speaking, macroscopic models are more amenable to rigorous traveling-wave analyses, while the properties of traffic jams in microscopic models are usually investigated by direct numerical simulations or Monte–Carlo simulations. This paper focuses on the investigation of traffic jams in a microscopic model that accounts for the adjustment of headways of individual cars. Similar to many other models including [2, 6, 12], this model predicts the existence of stable free-flow solutions that can destabilize to give rise to traffic-jam solutions; in contrast to some of the earlier findings, we observe coexistence of several stable traffic-jams states. On the technical level, we show how bifurcation theory and continuation methods can be used to efficiently analyze and compute traveling waves in discrete systems.

One of the most simple, yet rich and widely used, microscopic traffic flow models is the optimal-velocity model introduced in [3]. We review a non-dimensionalized version of this model and refer to [10, §I+VII] for the relation of the non-dimensional parameters used below to the physical parameters arising in actual traffic flows. In this model, each driver adjusts their acceleration to bring their velocity to an optimal velocity that depends on the headway, that is the distance from the vehicle in front. If $p_n(t)$ is the position of the nth vehicle, then the model is given by

$$\delta \ddot{p}_n = \mathcal{V}(p_{n+1} - p_n - \bar{s}) + v_0 - \dot{p}_n, \tag{1.1}$$

where the dot symbol means d/dt. Here, v_0 is related to a common optimal velocity; the adjustment $\mathcal{V}$ depends on the difference of the headway $p_{n+1} - p_n$ from an optimal headway $\bar{s}$ that encompasses the car length plus a safety distance: we will assume throughout this paper that $\mathcal{V}'(u) > 0$ and will use the concrete choice $\mathcal{V}(u) = \tanh(u)$ in our numerical computations. The parameter δ is a dimensionless reaction time that depends on the physical reaction time, the optimal velocity, and the car length as described in [10, §I]. Several works addressed extensions of (1.1): we mention here [7, 8], where drivers react also to the preceding car, and [9, 10] in which the optimal headway $\bar{s}$ varied deterministically or stochastically in time.

In this paper, we consider the situation of N cars driving on a circular road of fixed length L and aim to study the effects of allowing drivers to adjust their velocity using not just the distance but also the relative velocity to the car in front. To accomplish this, we associate with each driver a new dynamic variable $s_n(t)$, the individual target headway and augment the optimal-velocity equation (1.1) with a second equation that describes the evolution of $s_n(t)$. The resulting model is given by

$$\begin{aligned} \delta \ddot{p}_n &= \mathcal{V}(p_{n+1} - p_n - s_n) + v_0 - \dot{p}_n \\ \alpha \dot{s}_n &= \bar{s} - s_n - \beta \left(\dot{p}_{n+1} - \dot{p}_n \right), \end{aligned} \tag{1.2}$$

where the term $\bar{s} - s_n$ describes the relaxation of the individual target headway $s_n(t)$

to the optimal headway $\bar{s}$, while the term $\beta(\dot{p}_{n+1}-\dot{p}_n)$ takes into account that drivers may increase speed if the car in front does so: the parameter α is a measure of the overall adjustment time of the individual headways, while β measures how proactively drivers react to changes of the relative velocity. More specifically, for $\beta > 0$, the target headway s_n, which enters as an argument into the optimal-velocity function, is decreased if the car in front is driving faster, thus resulting in an increase of the optimal velocity on the nth car. The advantage of this model is that it allows us to change the behavior of drivers by varying the parameter α and β: as we will see, the resulting traffic flow depends strongly on the parameters α and β. We remark that setting $(\alpha, \beta) = 0$ recovers the standard optimal-velocity model (1.1).

We will show that the model (1.2) admits a free-flow solution where cars move with identical speeds and distances: the stability of this solution depends on the parameters (α, β). We will also discuss the existence, uniqueness, and stability of rotating-wave solutions that correspond to traffic jams. We focus primarily on the case when the optimal headway $\bar{s}$ coincides with the average distance L/N between cars; our main findings in this situation can be summarized briefly as follows:

- there is a bounded region in the (α, β)-plane in which the free-flow solution is stable;
- the boundary of the free-flow stability region is given by supercritical bifurcations to k-jam solutions;
- in the region of instability of the free-flow, k-jam solutions for different k can coexist;
- regions of bistability of free-flow and traffic-jam solutions do not exist;
- the basins of attraction of different k-jam solutions are separated by the stable manifolds of modulated jam solutions.

The remainder of the paper is organized as follows. In §2, we present a more convenient formulation of our model. We then discuss the stability of the free-flow solution in §3 and the existence and stability of traveling waves in §4. The interpretation of our findings for flux and energy consumption is discussed in §5, and we end in §6 with conclusions and an outlook.

2. Set-up. Recall that we aim to study the extended optimal-velocity system

$$\begin{aligned} \delta\ddot{p}_n &= \mathcal{V}(p_{n+1} - p_n - s_n) + v_0 - \dot{p}_n \\ \alpha\dot{s}_n &= \bar{s} - s_n - \beta(\dot{p}_{n+1} - \dot{p}_n) \end{aligned} \tag{2.1}$$

with periodic boundary conditions

$$p_{n+N} = p_n + L, \qquad s_{n+N} = s_n$$

for the positions p_n and the headways s_n for N cars traveling on a circular road of length L. If all cars are spaced equally along the road, the distance between consecutive cars is L/N. It will be convenient to use this fact by introducing the quantities

$$d_n = p_{n+1} - p_n - \frac{L}{N}, \qquad h_n = s_n - \bar{s}, \qquad \ell = \frac{L}{N} - \bar{s}.$$

In particular, d_n is the distance between consecutive cars minus the average distance L/N of cars, the variable h_n describes the difference between individual and optimal headways, and the parameter ℓ can be thought of as measuring overall traffic volume; note that $\ell = L/N - \bar{s} < 0$ corresponds to high traffic volume since the optimal headway distance $\bar{s}$ is larger than the average distance L/N of cars allowed. In these new variables, and written as a first-order system, (2.1) becomes

$$\begin{pmatrix} \dot{d}_n \\ \dot{v}_n \\ \dot{h}_n \end{pmatrix} = \begin{pmatrix} v_n \\ \frac{1}{\delta}\left[\mathcal{V}(d_{n+1} - h_{n+1} + \ell) - \mathcal{V}(d_n - h_n + \ell) - v_n\right] \\ -\frac{1}{\alpha}\left(h_n + \beta v_n\right) \end{pmatrix} \tag{2.2}$$

with the conditions

$$\sum_{k=1}^{N} d_k = 0, \quad d_{n+N} = d_n, \quad h_{n+N} = h_n \quad \forall n.$$

It is this formulation that we will use in the forthcoming analysis.

3. The free-flow solution. Equation (2.2) admits the stationary free-flow solution $(d_n, v_n, h_n) = (0, 0, 0)\ \forall n$, where all cars move with constant velocity and equal spacing between neighboring cars. In this section, we discuss the stability of this solution and the bifurcations it may undergo as the system's parameters are changed.

3.1. Stability analysis. Stability of the free-flow solution can be assessed by considering the linearization of the first-order system (2.2) about the free-flow solution. It is convenient to use a Fourier series formulation for this purpose. Writing

$$u_n = \begin{pmatrix} d_n \\ v_n \\ h_n \end{pmatrix} \in \mathbb{R}^3 \tag{3.1}$$

and taking the Fourier transform

$$u_n = \sum_{k=-\frac{N}{2}+1}^{\frac{N}{2}} U_k e^{2\pi i k n/N}, \quad U_k \in \mathbb{C}^3, \quad U_{-k} = \overline{U}_k, \tag{3.2}$$

the system (2.2) reduces to the system

$$\dot{U}_k = A_k U_k + \mathcal{F}_k(U), \qquad U = (U_{\frac{N}{2}+1}, \ldots, U_{\frac{N}{2}}) \in \mathbb{C}^{3N}, \quad k = -\frac{N}{2}+1, \ldots, \frac{N}{2}, \tag{3.3}$$

where the matrices $A_k \in \mathbb{C}^{3\times 3}$ are given by

$$A_k = \begin{pmatrix} 0 & 1 & 0 \\ \dfrac{\mathcal{V}'(\ell)}{\delta}\left(e^{2\pi i k/N} - 1\right) & -\dfrac{1}{\delta} & \dfrac{\mathcal{V}'(\ell)}{\delta}\left(1 - e^{2\pi i k/N}\right) \\ 0 & -\dfrac{\beta}{\alpha} & -\dfrac{1}{\alpha} \end{pmatrix}, \tag{3.4}$$

and the nonlinearity is at least quadratic so that $\mathcal{F}_k(U) = O(|U|^2)$. In particular, the linearization of the first-order system (2.2) about the free-flow solution reduces to a system of N eigenvalue problems for the 3×3 matrices A_k; we remark that $\beta = 0$ recovers the stability matrices of the free flow in the original model (1.1). The eigenvalues λ of the matrices A_k are given by solutions of

$$\left(\delta\lambda^2 + 1 - \mathcal{V}'(\ell)\gamma_k\right)(1 + \alpha\lambda) - \beta\lambda\gamma_k = 0, \tag{3.5}$$

where

$$\gamma_k = e^{2\pi i k/N} - 1.$$

To detect instabilities, we use the condition Re(λ)=0 and write $\lambda = i\nu$ with ν real; substitution into (3.5) results in the two equations

$$\begin{aligned} -(\alpha+\delta)\nu^2 + \mathcal{V}'(\ell)((\alpha-\beta)\nu\sin(2\pi k/N) - (\cos(2\pi k/N) - 1)) &= 0 \\ \nu\left(1 - \alpha\delta\nu^2\right) + \mathcal{V}'(\ell)((\alpha-\beta)\nu(\cos(2\pi k/N) - 1) - \sin(2\pi k/N)) &= 0. \end{aligned} \tag{3.6}$$

Solutions with $k \neq 0$ correspond to Hopf instabilities as ν is then necessarily nonzero. Tedious but straightforward calculations for (3.5) show that the free-flow solution is stable when

$$\delta < \delta_c \coloneqq \frac{1}{2\mathcal{V}'(\ell)} + \beta. \tag{3.7}$$

For the opposite inequality, the free-flow solution is unstable with respect to the linear modes k with $|k| \leq k_c$: the critical index $k_c > 0$ satisfies the equation

$$\cos^2\left(\frac{\pi k_c}{N}\right) = \frac{z}{2\delta\mathcal{V}'(\ell)}, \tag{3.8}$$

where the coefficient z is the positive root of the equation

$$c_2 z^2 - c_1 z + c_0 = 0, \tag{3.9}$$

with the coefficients c_j given by

$$\begin{aligned}
c_0 &= \delta\left(\alpha+\delta+2\mathcal{V}'(\ell)(\alpha^2+\alpha\beta+\beta\delta)\right)^2\\
c_1 &= 2\mathcal{V}'(\ell)\left(\alpha^4+2\alpha^3(\beta+\delta)+\alpha^2\left(\beta^2+5\beta\delta+2\delta^2\right)+\alpha\beta\delta(3\beta+\delta)+\beta^2\delta^2\right)\\
&\quad+(\alpha+\delta)\left(2\alpha^2+\alpha(\beta+\delta)+\delta(\beta+\delta)\right)+\alpha\delta(\alpha+\beta)^3\\
c_2 &= \alpha\left((2\alpha+\beta)(\alpha+\beta+\delta)+2\mathcal{V}'(\ell)(\alpha+\beta)^3\right).
\end{aligned} \tag{3.10}$$

If drivers ignore the relative velocity to the preceding car, that is when $\beta = 0$, we have $z = 1$ and find that the free flow is stable provided the reaction time δ satisfies

$$\delta < \delta_0 = \frac{1}{2\mathcal{V}'(\ell)}, \tag{3.11}$$

while the free flow is unstable for the opposite inequality. More generally, for weak proactiveness ($|\beta| \ll 1$) and in the close vicinity of the threshold ($|\delta - \delta_c| \ll 1$), equation (3.8) for the critical wave number k_c reduces to

$$\cos^2\left(\frac{\pi k_c}{N}\right) = \frac{\delta_c}{\delta}, \tag{3.12}$$

and modes with $|k| > k_c$ are linearly stable, while the other modes are unstable for the free flow; this agrees with the stability criteria of the free-flow solution of the original model (1.1).

3.2. Numerical results. The analysis in the preceding section does not provide explicit conclusions for $\beta > 0$, and we therefore trace out the stability and instability regions for the optimal-velocity model for the function

$$\mathcal{V}(u) = \tanh u \tag{3.13}$$

using numerical computations.

The domain of instability of the free-flow solution in (δ, β)-space is presented in Figure 3.1. These results demonstrate that the unreasonable driving behavior of negative feedback ($\beta < 0$), where the target headway decreases when the relative velocity of two neighboring cars increases, destabilizes the free flow, whilst positive feedback makes the free-flow solution more stable. Increasing the adjustment time α similarly enhances free-flow stability.

Next, we trace out instability curves of the free flow in (α, β)-space. A secant continuation solver was used to determine the free-flow stability boundary numerically in Matlab for the case of $\delta = 0.55$. This value of δ was used in all remaining numerical computations in the paper. The eigenvalues of the matrices A_k were continued to trace out the kth mode stability curves in the (α, β) plane. These curves represent

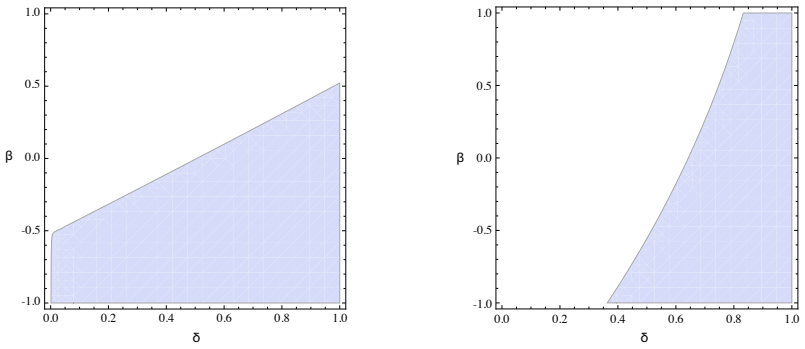

Fig. 3.1: The free-flow solution is unstable in the shaded parameter region, where δ is the non-dimensional reaction time and β is the feedback parameter. We set $\ell = 0$ and show the cases $\alpha = 1$ (left panel) and $\alpha = 10$ (right panel).

the location of Hopf bifurcations from the free flow, as for each mode the free flow loses stability as a complex conjugate pair of eigenvalues crosses the imaginary axis.

The resulting bifurcation curves for $k = 1, \ldots, 6$ are shown in Figure 3.2 for $\ell = 0$ and $\ell = 0.22$ for three different values of the number N of cars. These results show that the free flow, at least its approximation by the first six Fourier modes, is stable in a region in the lower left corner of each diagram, that is, for smaller values of (α, β), and that the boundary of this region is composed of segments of the kth mode instability curves along which Hopf bifurcations occur. It can also be seen that the shape of the stability region for a given mode changes in N. As N increases, more of the stability curves appear to fold back to the left. Upon further investigation, we found additional kth mode stability boundaries which appear in the region of negative β. This is illustrated in Figure 3.3 where both stability boundaries for $k = 2$ are shown for four different values of N in the case of $\ell = 0$. At some critical value of N, the stability region splits into two disconnected components, and hence the fold appears in the region of positive β. For a given k, we find this critical value $N = N_k$ by determining when the stability boundary crosses the α-axis. Considering the matrices A_k for $\beta = 0$, we see that nonzero eigenvalues λ satisfy

$$\lambda\left(\lambda + \frac{1}{\delta}\right) - \frac{\mathcal{V}'(\ell)}{\delta}\left(e^{2\pi i k/N_k} - 1\right) = 0. \tag{3.14}$$

Taking $\lambda = \mu + i\nu,\ \mu, \nu \in \mathbb{R}$, we see that $\mu = 0$ when

$$\mathrm{Re}\left(\sqrt{1 + 4\delta\mathcal{V}'(\ell)\left(e^{2\pi i k/N_k} - 1\right)}\right) = 1. \tag{3.15}$$

A short calculation shows that this is equivalent to the condition

$$\cos\left(\frac{2\pi k}{N_k}\right) = -1 + \frac{1}{\delta \mathcal{V}'(\ell)}. \tag{3.16}$$

We will discuss the traffic patterns that emerge at the Hopf instability curves in the next section.

4. Rotating waves. In this section, we discuss which nonlinear structures emerge at the Hopf bifurcations of the free-flow solution. We restrict ourselves to the case $\ell = 0$ where the optimal headway $\bar{s}$ coincides with the average distance between cars. We will show first that the bifurcating patterns in this case are rotating waves that correspond to traffic jams: if the kth mode of the free flow destabilizes, the resulting jam solutions will have k maxima, and we will refer to these waves as k-jam solutions. After discussing their existence near onset, we present the results of numerical computations, where we trace the k-jam solutions to finite amplitude. We also determine the stability of the traffic-jam solutions and analyze the bifurcations that occur when they destabilize.

4.1. Existence of jam solutions. Recall that we consider the system

$$\begin{pmatrix} \dot{d}_n \\ \dot{v}_n \\ \dot{h}_n \end{pmatrix} = \begin{pmatrix} v_n \\ \frac{1}{\delta}\left[\mathcal{V}(d_{n+1} - h_{n+1} + \ell) - \mathcal{V}(d_n - h_n + \ell) - v_n\right] \\ -\frac{1}{\alpha}\left(h_n + \beta v_n\right) \end{pmatrix} \tag{4.1}$$

with indices taken modulo N. This system is equivariant under shifts in the index n, that is, it admits the $\mathbb{Z}_N$ symmetry generated by $\kappa : \mathbb{R}^{3N} \to \mathbb{R}^{3N}$ given by $[\kappa(d, v, h)]_n = (d_{n-1}, v_{n-1}, h_{n-1})$ for $(d, v, h) \in \mathbb{R}^{3N}$ with indices taken modulo N. If one of the matrices A_k given in (3.4) has a purely imaginary eigenvalue $\lambda = i\omega$ for some $k \neq 0$ with corresponding eigenvector $\xi \in \mathbb{C}^3$, then the eigenspace of the linearization about the original system (4.1) corresponding to $i\omega$ is spanned by the vectors

$$(d_n, v_n, h_n) = \xi e^{2\pi i k n/N}, \quad n = 1, \ldots, N, \tag{4.2}$$

and the $\mathbb{Z}_N$ symmetry acts according to

$$\kappa : \xi \longrightarrow \xi e^{2\pi i k/N}, \tag{4.3}$$

which leaves the eigenspace invariant. Therefore, [11, Theorem XVII.8.2] predicts the bifurcation of rotating waves with spatial symmetry $\mathbb{Z}_m$ where $m = \gcd(k, N)$ is the greatest common divisor of k and N: these waves are of the form $(d_n(t), v_n(t), h_n(t))$ with

$$(d_n(t), v_n(t), h_n(t)) = (d_*(n - ct), v_*(n - ct), h_*(n - ct))$$

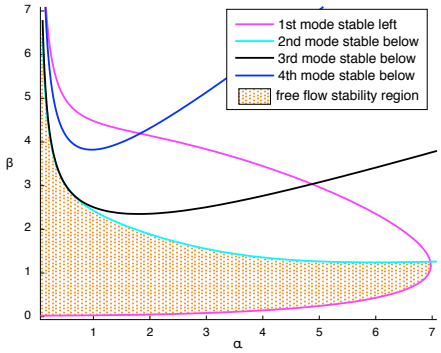

(a) $N = 15, \ell = 0$

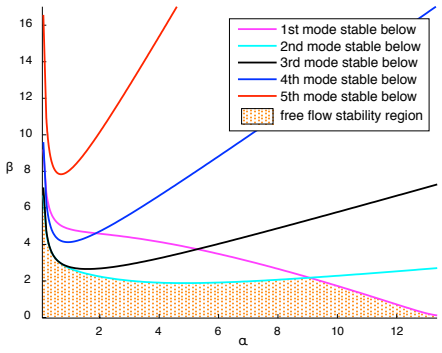

(b) $N = 15, \ell = 0.22$

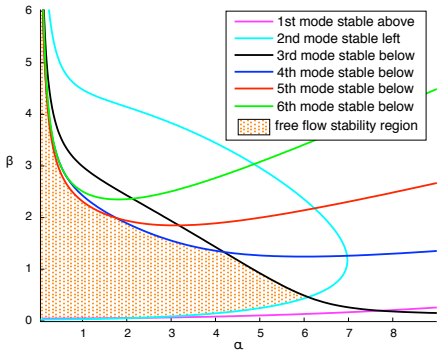

(c) $N = 30, \ell = 0$

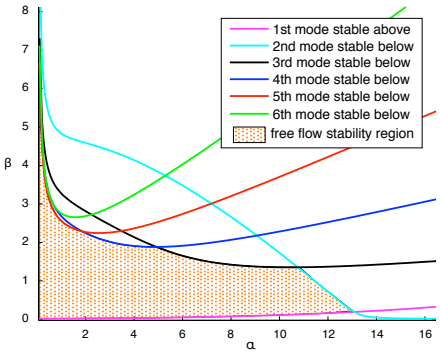

(d) $N = 30, \ell = 0.22$

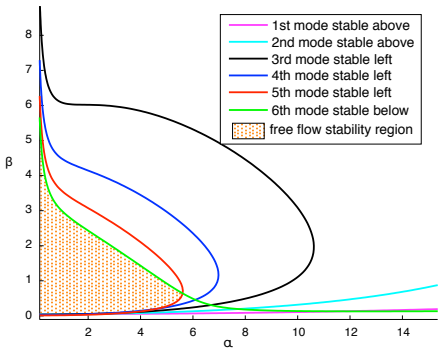

(e) $N = 60, \ell = 0$

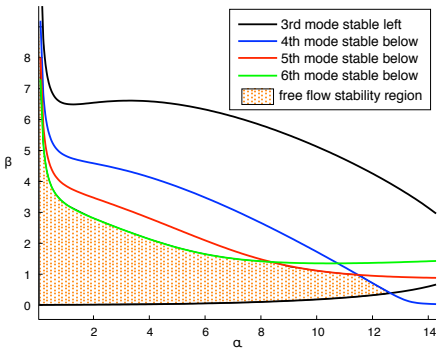

(f) $N = 60, \ell = 0.22$

Fig. 3.2: Shown are the curves in (α, β)-space at which the kth mode of the free-flow solution destabilizes for $k = 1, \ldots, 6$. The number N of cars and the discrepancy ℓ between mean distance between cars and the optimal headway varies in the panels as indicated. We set $\delta = 0.55$. The region of free-flow stability for the approximation by the first six modes is shaded.

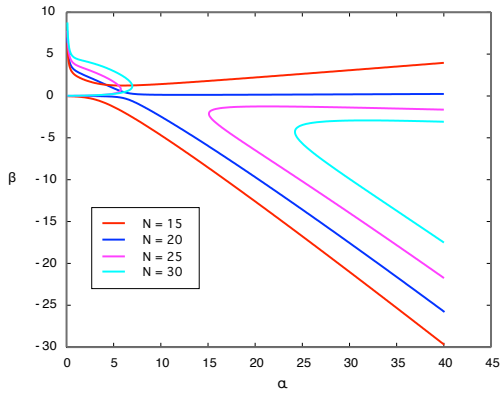

Fig. 3.3: Shown is the collision and rearrangement of two distinct instability curves for the $k = 2$ mode as N varies with $\ell = 0$ and $\delta = 0.55$.

for appropriate N-periodic functions $(d_*, v_*, h_*)(x)$; we have $\kappa^m(d, v, h)(t) = (d, v, h)(t)$ for all times t, reflecting the spatial symmetry $\mathbb{Z}_m$.

To compute traffic-jam solutions numerically, we again set $\mathcal{V}(u) = \tanh(u)$ and $\ell = 0$, and we fix $\delta = 0.55$. Substitution of the rotating-wave ansatz

$$(d_n(t), v_n(t), h_n(t)) = (d(n - ct), v(n - ct), h(n - ct))$$

into (4.1) results in the delay differential equations

$$\begin{aligned} -cd'(x) &= v(x) \\ -\delta c v'(x) &= \tanh(d(x+1) - h(x+1)) - \tanh(d(x) - h(x)) - v(x) \\ -c\alpha h'(x) &= -h(x) - \beta v(x), \end{aligned} \tag{4.4}$$

where $'$ denotes the derivative with respect to the traveling wave variable $x = n - ct$. We seek N-periodic solutions $(d, v, h)(x)$ of this system and point out that the wave speed c is a variable that needs to be solved for as part of (4.4). To find these structures numerically, we used branch switching from the free flow at the Hopf bifurcation points discussed above. Figure 4.1 shows k-jam profiles for $k = 1, 2, 3, 4$ found numerically for $N = 30$ and illustrates their spatial symmetry $\mathbb{Z}_m$ where $m = \gcd(k, N)$. Plots of the wavespeed c as a function of the parameter β for k-jam solutions with $k = 2, 3, 4$ are shown in Figure 4.2 for two different values of α.

We emphasize that the Hopf bifurcations we computed are all supercritical. In particular, free-flow and traffic-jam solutions never coexist, though different traffic-jam solutions can exist simultaneously.

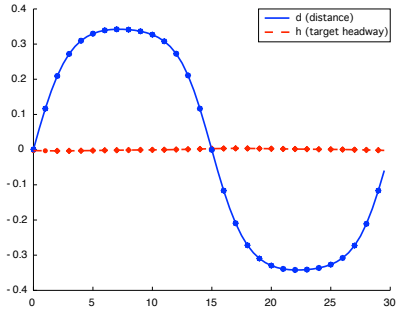

(a) $(\alpha, \beta) = (4, 0.05)$, k=1

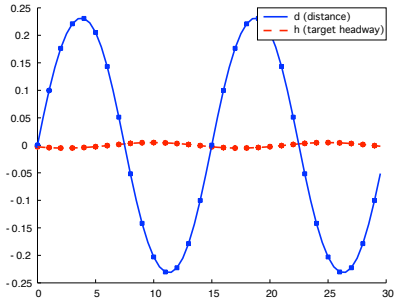

(b) $(\alpha, \beta) = (4, 0.1)$, k=2

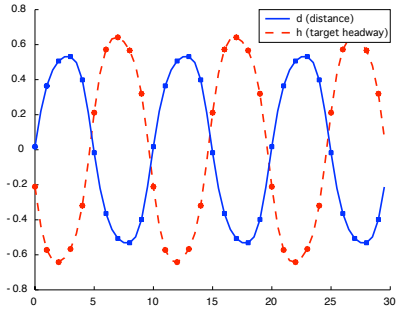

(c) $(\alpha, \beta) = (6, 1)$, k=3

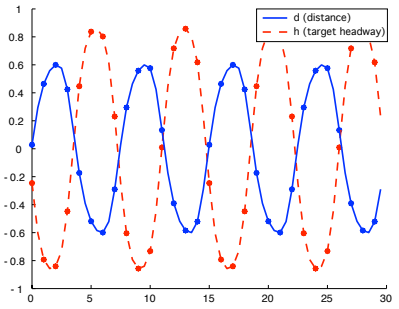

(d) $(\alpha, \beta) = (4, 6)$, k=4

Fig. 4.1: Example profiles of the k-jam rotating-wave solutions for $N = 30$; here the x-axis represents the car index. The solid lines show the continuous profiles found using the traveling-wave ansatz, and dots show the values taken at N equally spaced points to represent the individual cars. We found only symmetric continuous traveling-wave profiles but note that the discrete k-jam solutions should have spatial symmetry $\mathbb{Z}_m$ where $m = \gcd(k, N)$: this symmetry is apparent in the dotted profiles.

Finally, we also considered the mean-square headway

$$M(t) = \sum_{n=1}^{N} |d_n(t)|^2, \tag{4.5}$$

which is a measure of the total deviation from the free flow. This quantity vanishes identically for the free-flow solution. Figure 4.3 shows the mean-square headway, averaged over one period, as a function of β for the 1-jam and 2-jam solutions. Note that the mean-square headway curves of 1-jams and 2-jams approach zero at their respective bifurcation points from the free-flow solution.

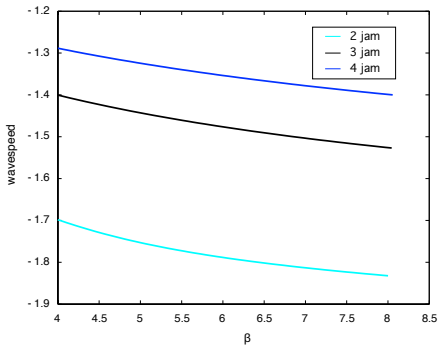

(a) $\alpha = 4$

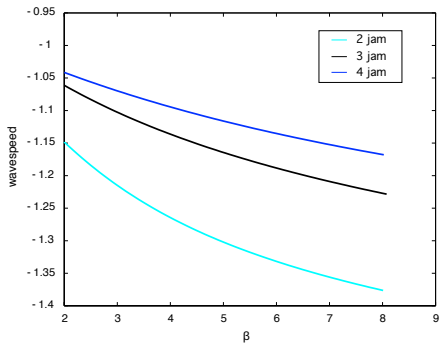

(b) $\alpha = 8$

Fig. 4.2: Plotted is the wavespeed c for a sample of k-jam solutions as a function of the parameter β.

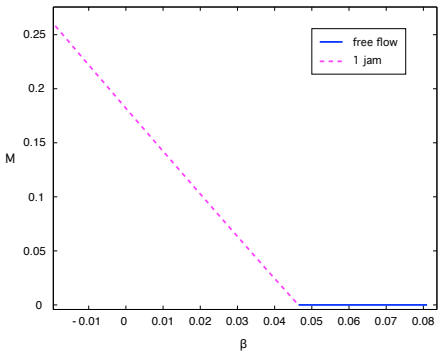

(a) $\alpha = 1$

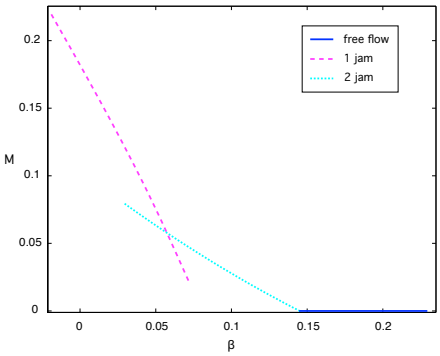

(b) $\alpha = 4$

Fig. 4.3: Plotted is the mean square headway M versus the parameter β for free flow and k-jam solutions in their respective regions of stability.

4.2. Stability. The stability of a rotating-wave solution (d_*, v_*, h_*) can be determined by linearizing (4.4) about (d_*, v_*, h_*) to get the differential operator $\mathcal{L}$ defined by

$$\mathcal{L}\begin{pmatrix}\tilde{d}\\ \tilde{v}\\ \tilde{h}\end{pmatrix} = c\begin{pmatrix}\tilde{d}_x\\ \tilde{v}_x\\ \tilde{h}_x\end{pmatrix} + \begin{pmatrix}\tilde{v}\\ \frac{1}{\delta}\left(\tanh'(d_*(x+1)-h_*(x+1))(\tilde{d}(x+1)-\tilde{h}(x+1)) - \tanh'(d_*(x)-h_*(x))(\tilde{d}-\tilde{h}) - \tilde{v}\right)\\ -\frac{1}{\alpha}\left(\tilde{h}+\beta\tilde{v}\right)\end{pmatrix}.$$

It is then not difficult to see that the spectrum of this operator on the space of $2\pi/N$-periodic functions $(\tilde{d}, \tilde{v}, \tilde{h})$ coincides with the Floquet spectrum of the rotating-wave

solution $(d_n, v_n, h_n)(t) = (d_*(n-ct), v_*(n-ct), h_*(n-ct))$ of (4.1); see, for instance, [4] for similar results.

To find the stability boundaries for a rotating-wave solution, we used a Matlab secant continuation solver to simultaneously solve the differential equation (4.4) for (d, v, h) and the eigenvalue equation

$$(\mathcal{L} - \lambda I) \begin{pmatrix} \tilde{d} \\ \tilde{v} \\ \tilde{h} \end{pmatrix} = 0$$

for $(\tilde{d}, \tilde{v}, \tilde{h}, \lambda)$. In carrying out the above calculations for k-jam rotating-wave solutions for $k = 1, \ldots, 6$, we find the stability boundaries shown in Figure 4.4. Along these curves, the rotating waves lose stability as a pair of complex conjugate eigenvalues cross the imaginary axis and thus they depict the location of Hopf bifurcations from the k-jam solutions described above. Note that these curves emerge from codimension-two points at which two different eigenvalues, corresponding to two different values of k, of the free flow cross the imaginary axis simultaneously.

We reiterate that free-flow and traffic-jam solutions cannot, apparently, coexist for $\ell = 0$, though different traffic-jam solutions can coexist; moreover, our stability computations indicate that there is multistability in that multiple k-jam solutions for different values of k can be simultaneously stable for the same parameter values. This was also confirmed in our direct numerical simulations which revealed that different initial data can evolve into different traffic-jam solutions. To understand what determines the boundaries of their respective basin of attraction, we focus in the next section on the aforementioned codimension-two points at which two different modes, associated with different values of k, of the free flow destabilize.

4.3. Hopf-Hopf mode interactions. We focus on the Hopf-Hopf mode interaction bifurcation points at which two different modes of the free-flow solution destabilize simultaneously. Two of these codimension-two points are visible in panels (1) and (2) of Figure 4.4. Hopf-Hopf interactions were studied analytically in [25]. As shown there (see also [13]), there are twelve possible generic unfoldings of this bifurcation: to determine which of these cases occurs in the traffic flow model, we derive the normal forms that govern the dynamics near these points. To complement this approach, we will also consider a low-dimensional Fourier-mode approximation that sheds additional light on the Hopf-Hopf mode interaction point shown in Figure 4.4(1).

4.3.1. Normal-form computation. To compute the normal form near Hopf-Hopf mode interaction points, we return to the system (4.1) with $\ell = 0$ and $\mathcal{V}(u) =$

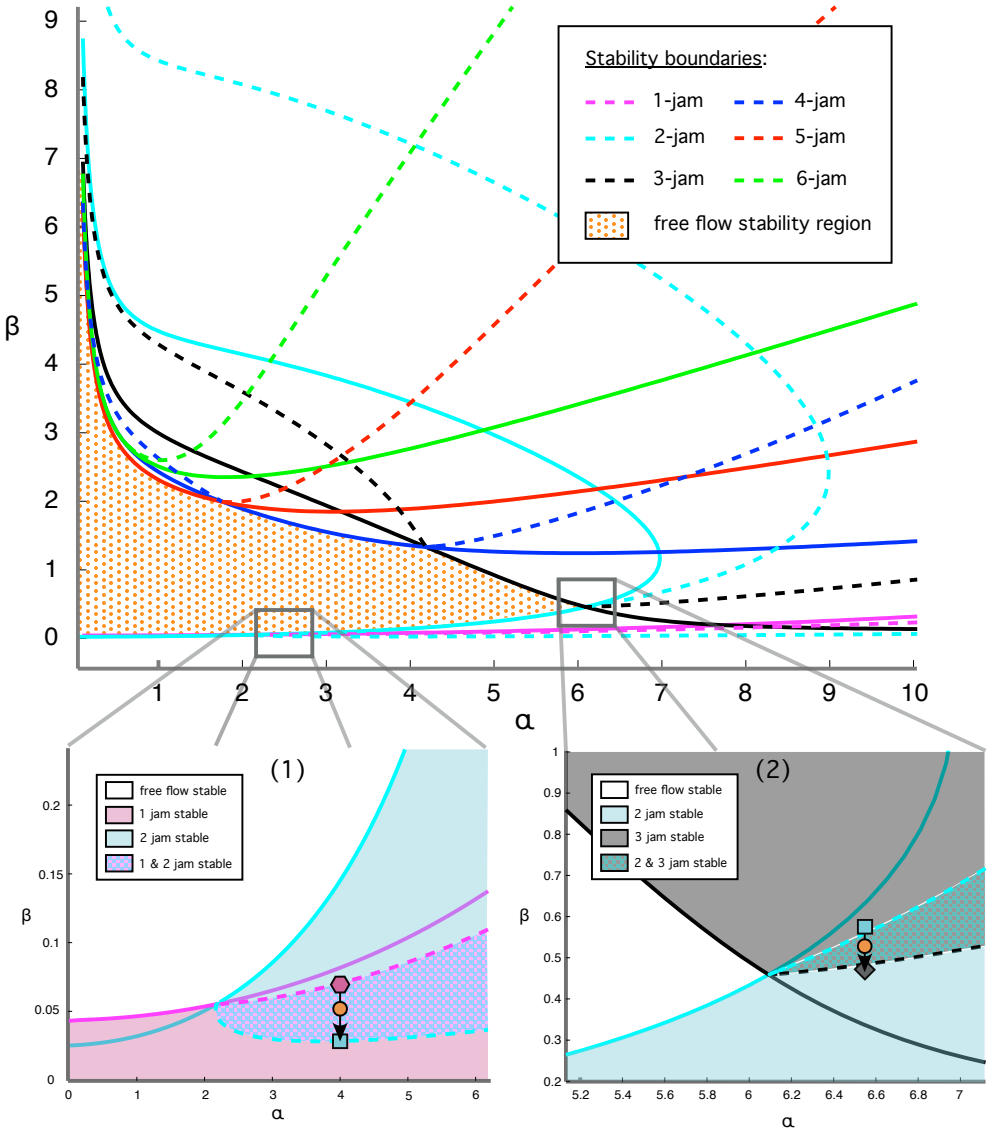

Fig. 4.4: Bifurcation diagram for $N = 30$. The colored shapes along the arrows in the two inset figures refer to the modulated-wave solutions found using the continuation scheme from §4.4.

$\tanh(u)$ given by

$$\begin{pmatrix} \dot{d}_n \\ \dot{v}_n \\ \dot{h}_n \end{pmatrix} = \begin{pmatrix} v_n \\ \frac{1}{\delta}\left[\tanh(d_{n+1} - h_{n+1}) - \tanh(d_n - h_n) - v_n\right] \\ -\frac{1}{\alpha}\left(h_n + \beta v_n\right) \end{pmatrix}. \tag{4.6}$$

Expanding the nonlinearity and substituting the Fourier series expansion (3.2), we arrive at the system (3.3)

$$\dot{U}_k = A_k U_k + \mathcal{F}_k(U), \qquad k = -\frac{N}{2}+1, \ldots, \frac{N}{2}. \tag{4.7}$$

We now compute the normal form for this system. Writing

$$U_k = \begin{pmatrix} D_k \\ V_k \\ H_k \end{pmatrix}, \tag{4.8}$$

we find that the nonlinearity $\mathcal{F}_k$ can now be written as

$$\mathcal{F}_k(U) = \begin{pmatrix} 0 \\ \mathcal{F}_{k,2}(U) \\ 0 \end{pmatrix}, \tag{4.9}$$

where

$$\mathcal{F}_{k,2}(U) = -\frac{\gamma_k}{3\delta} \sum_{k_1+k_2+k_3=k} (D_{k_1} - H_{k_1})(D_{k_2} - H_{k_2})(D_{k_3} - H_{k_3}) + O(|U|^5) \tag{4.10}$$

with

$$\gamma_k = e^{2\pi i k/N} - 1.$$

To investigate the Hopf-Hopf mode interaction of the free flow, we assume that at some critical parameter value $(\alpha, \beta) = (\alpha_c, \beta_c)$ the matrices A_{k_1} and A_{k_2} for two distinct fixed values k_1 and k_2 each have one eigenvalue on the imaginary axis, given by $\lambda_k = i\omega_k \in i\mathbb{R}$ for $k = k_1, k_2$, while their remaining eigenvalues lie in the open left half-plane. We also assume that the matrices A_k for $k \neq k_1, k_2$ have eigenvalues with strictly negative real part.

In particular, our system has a four-dimensional center manifold, and we now parametrize the flow on this center manifold. Denote by $\tilde{U}_{k_1}^{(1)}$ the eigenvector of A_{k_1} corresponding to the eigenvalue $i\omega_1$ and by $\tilde{U}_{k_1}^{(2)}$ and $\tilde{U}_{k_1}^{(3)}$ the other two eigenvectors of A_{k_1}. Similarly, let $\tilde{U}_{k_2}^{(1)}$ the eigenvector of A_{k_2} corresponding to the eigenvalue $i\omega_2$ and denote by $\tilde{U}_{k_2}^{(2)}$ and $\tilde{U}_{k_2}^{(3)}$ the other two eigenvectors of A_{k_2}. Finally, we will make use of the eigenvectors $\tilde{W}_k^{(1)}$ belonging to the eigenvalues $-i\omega_k$ of the adjoint matrices $\overline{A_k}^t$ for $k = k_1, k_2$.

Solutions on the four-dimensional center manifold can then be written as

$$\begin{cases} U_{k_1} &= \epsilon_1(t)\tilde{U}_{k_1}^{(1)} + O(|\epsilon|^2)\tilde{U}_{k_1}^{(2)} + O(|\epsilon|^2)\tilde{U}_{k_1}^{(3)} \\ U_{k_2} &= \epsilon_2(t)\tilde{U}_{k_2}^{(1)} + O(|\epsilon|^2)\tilde{U}_{k_2}^{(2)} + O(|\epsilon|^2)\tilde{U}_{k_2}^{(3)} \\ U_k &= O(|\epsilon|^2), \qquad |k| \neq k_1, k_2. \end{cases} \tag{4.11}$$

We remark that the real part of the amplitudes ϵ_1 and ϵ_2 determine the profile of solutions, whereas their imaginary parts corresponds to space-time shifts; see [13, 25]. Thus, we focus our attention on the equations for the real parts, which can be derived as follows. Substituting the expression (4.11) into (4.7), using the form of the nonlinearity from (4.10), and finally taking the scalar product of the resulting equation with the adjoint eigenvectors $\tilde{W}_k^{(1)}$ for $k = k_1, k_2$ yields the system

$$\begin{aligned} \dot{r}_1 &= r_1 \left[a_{11}(\alpha - \alpha_c) + a_{12}(\beta - \beta_c) + b_{11} r_1^2 + b_{12} r_2^2 \right] + O(|r|^5) \\ \dot{r}_2 &= r_2 \left[a_{21}(\alpha - \alpha_c) + a_{22}(\beta - \beta_c) + b_{21} r_1^2 + b_{22} r_2^2 \right] + O(|r|^5) \end{aligned} \tag{4.12}$$

for $r_j = \operatorname{Re} \epsilon_j$ with $j = 1, 2$. The coefficients appearing in this equation are given by

$$\begin{aligned} a_{11} &= \operatorname{Re} \frac{\left\langle \tilde{W}_{k_1}^{(1)}, \frac{dA_{k_1}}{d\alpha}\Big|_{(\alpha_c,\beta_c)} \tilde{U}_{k_1}^{(1)} \right\rangle}{\left\langle \tilde{W}_{k_1}^{(1)}, \tilde{U}_{k_1}^{(1)} \right\rangle} \qquad a_{12} = \operatorname{Re} \frac{\left\langle \tilde{W}_{k_1}^{(1)}, \frac{dA_{k_1}}{d\beta}\Big|_{(\alpha_c,\beta_c)} \tilde{U}_{k_1}^{(1)} \right\rangle}{\left\langle \tilde{W}_{k_1}^{(1)}, \tilde{U}_{k_1}^{(1)} \right\rangle} \\ a_{21} &= \operatorname{Re} \frac{\left\langle \tilde{W}_{k_2}^{(1)}, \frac{dA_{k_2}}{d\alpha}\Big|_{(\alpha_c,\beta_c)} \tilde{U}_{k_2}^{(1)} \right\rangle}{\left\langle \tilde{W}_{k_2}^{(1)}, \tilde{U}_{k_2}^{(1)} \right\rangle} \qquad a_{22} = \operatorname{Re} \frac{\left\langle \tilde{W}_{k_2}^{(1)}, \frac{dA_{k_2}}{d\beta}\Big|_{(\alpha_c,\beta_c)} \tilde{U}_{k_2}^{(1)} \right\rangle}{\left\langle \tilde{W}_{k_2}^{(1)}, \tilde{U}_{k_2}^{(1)} \right\rangle} \end{aligned} \tag{4.13}$$

and

$$\begin{aligned} b_{11} &= -\operatorname{Re} \left[\frac{\gamma_{k_1}}{\delta} \frac{\overline{\tilde{W}}_{k_1,2}^{(1)} \left| \tilde{D}_{k_1}^{(1)} - \tilde{H}_{k_1}^{(1)} \right|^2 \left(\tilde{D}_{k_1}^{(1)} - \tilde{H}_{k_1}^{(1)} \right)}{\left\langle \tilde{W}_{k_1}^{(1)}, \tilde{U}_{k_1}^{(1)} \right\rangle} \right] \\ b_{12} &= -\operatorname{Re} \left[\frac{2\gamma_{k_1}}{\delta} \frac{\overline{\tilde{W}}_{k_1,2}^{(1)} \left| \tilde{D}_{k_2}^{(1)} - \tilde{H}_{k_2}^{(1)} \right|^2 \left(\tilde{D}_{k_1}^{(1)} - \tilde{H}_{k_1}^{(1)} \right)}{\left\langle \tilde{W}_{k_1}^{(1)}, \tilde{U}_{k_1}^{(1)} \right\rangle} \right] \\ b_{21} &= -\operatorname{Re} \left[\frac{2\gamma_{k_2}}{\delta} \frac{\overline{\tilde{W}}_{k_2,2}^{(1)} \left| \tilde{D}_{k_1}^{(1)} - \tilde{H}_{k_1}^{(1)} \right|^2 \left(\tilde{D}_{k_2}^{(1)} - \tilde{H}_{k_2}^{(1)} \right)}{\left\langle \tilde{W}_{k_2}^{(1)}, \tilde{U}_{k_2}^{(1)} \right\rangle} \right] \\ b_{22} &= -\operatorname{Re} \left[\frac{\gamma_{k_2}}{\delta} \frac{\overline{\tilde{W}}_{k_2,2}^{(1)} \left| \tilde{D}_{k_2}^{(1)} - \tilde{H}_{k_2}^{(1)} \right|^2 \left(\tilde{D}_{k_2}^{(1)} - \tilde{H}_{k_2}^{(1)} \right)}{\left\langle \tilde{W}_{k_2}^{(1)}, \tilde{U}_{k_2}^{(1)} \right\rangle} \right], \end{aligned} \tag{4.14}$$

where we used the notation

$$\tilde{U}_{k_j}^{(1)} = \begin{pmatrix} \tilde{D}_{k_j}^{(1)} \\ \tilde{V}_{k_j}^{(1)} \\ \tilde{H}_{k_j}^{(1)} \end{pmatrix}, \qquad \tilde{W}_{k_j}^{(1)} = \begin{pmatrix} \tilde{W}_{k_j,1}^{(1)} \\ \tilde{W}_{k_j,2}^{(1)} \\ \tilde{W}_{k_j,3}^{(1)} \end{pmatrix}$$

for $j = 1, 2$.

While it it not possible to evaluate the coefficients analytically, we can compute their values numerically by computing the eigenvectors and adjoint eigenvectors of

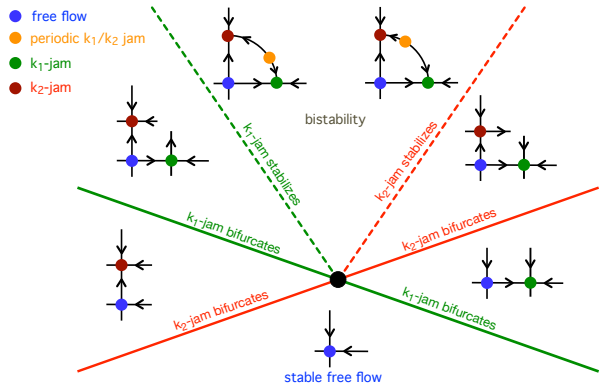

Fig. 4.5: A sketch of the bifurcation diagram of the normal form (4.12) is shown that corresponds to the regions in the insets of Figure 4.4. Note that the insets (1) and (2) in Figure 4.4 are qualitatively identical and correspond to the bifurcation diagram shown here with $(k_1, k_2) = (1, 2)$ and $(k_1, k_2) = (2, 3)$ respectively.

A_{k_j} numerically and substituting into the above expressions. For the mode interaction points of modes $(k_1, k_2) = (1, 2)$ and $(k_1, k_2) = (2, 3)$, we obtain the following coefficients:

Codim-2	a_{11}	a_{12}	a_{21}	a_{22}	b_{11}	b_{12}	b_{21}	b_{22}
$(k_1, k_2) = (1, 2)$	0.0003	-0.033	0.002	-0.069	-0.0209	-0.037	-0.15	-0.07
$(k_1, k_2) = (2, 3)$	0.002	-0.006	0.001	0.0038	-0.0773	-0.132	-0.26	-0.11

Using the normal form, we can then compute the slopes of the stability boundaries for the free-flow and k-jam solutions, which are shown in Figure 4.4. While there are several possible cases for the unfolding of (4.12) depending on the relative signs of the coefficients b_{ij}, we encountered only one particular unfolding, which is shown in Figure 4.5: the diagram shown in Figure 4.5 is indeed one of the twelve possible generic unfoldings of this bifurcation: it corresponds, up to time reversal, to [13, case Ib and Figure 7.5.2].

Based on the interpretation of r_1 and r_2 as the real amplitudes of the modes with wave numbers k_1 and k_2, respectively, we have the following interpretation of the solutions (r_1, r_2) of the normal form (4.12) and the bifurcation diagram shown in Figure 4.5. Equilibria of (4.12) with $r_2 = 0$ correspond to k_1-jam solutions, while equilibria with $r_1 = 0$ correspond to k_2-jam solutions. Finally, we see that equilibria that have $r_1, r_2 \neq 0$ bifurcate in a Hopf bifurcation from the k_1-jam solution and end, again at a Hopf bifurcation, at the k_2-jam solution. General theory outlined, for instance, in [21, Corollary 1] predicts that these bifurcating equilibria with $r_1, r_2 \neq 0$

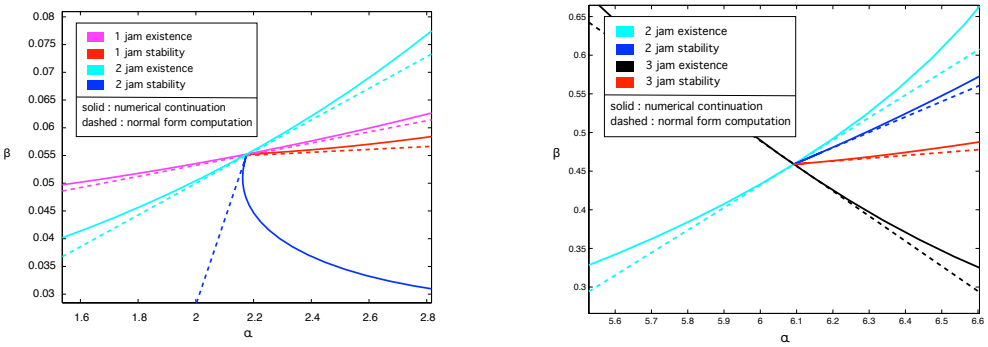

Fig. 4.6: Shown is a comparison of the predictions from the normal-form analysis and the results of numerical continuation for the two Hopf-Hopf mode interaction points for modes $k = 1, 2$ and $k = 2, 3$, respectively, shown in panels (1) and (2) of Figure 4.4.

correspond to modulated rotating waves of the original system (4.6). More precisely, they correspond to solutions of the form

$$(d_n, v_n, h_n)(t) = (d_*(n - ct, \omega t), v_*(n - ct, \omega t), h_*(n - ct, \omega t)) \tag{4.15}$$

where $(d_*, v_*, h_*)(x, \tau)$ is N-periodic in x and 2π-periodic in τ, and where (c, ω) depend on (α, β).

We compared the results of the numerical continuation with the results of the normal-form analysis in the regions near the Hopf-Hopf mode interaction points shown in the two insets of Figure 4.4. The stability lines computed from the normal-form computations are pictured along with the numerical results in Figure 4.6. It can be seen that there is good agreement between the numerics and the analysis in a neighborhood of the bifurcation points. In §4.4, we will calculate the modulated waves (4.15) directly for the original full problem (4.6).

4.3.2. Low-dimensional Fourier-series approximation. To derive a low-dimensional ODE that reflects the dynamics near a Hopf-Hopf mode interaction point, we again restrict to the case $\ell = 0$. Using equation (2.1), we see that the quantities $q_n(t) = d_n(t) - h_n(t)$ then satisfy the system

$$\begin{aligned} \delta\ddot{q}_n + \dot{q}_n + \delta\ddot{h}_n + \dot{h}_n &= \mathcal{V}(q_{n+1}) - \mathcal{V}(q_n) \\ (\alpha + \beta)\dot{h}_n + h_n + \beta\dot{q}_n &= 0 \end{aligned} \tag{4.16}$$

with periodic boundary conditions of the form $q_{n+N} = q_n$ and $h_{n+N} = h_n$ for all t and n. The free-flow solution is now given by $(q_n, h_n) \equiv 0$ for all n. We are interested in small-amplitude solutions. Instead of considering the function $\mathcal{V}(q) = \tanh(q)$, we use its cubic approximation $\mathcal{V}(q) = q - \frac{1}{3}q^3$.

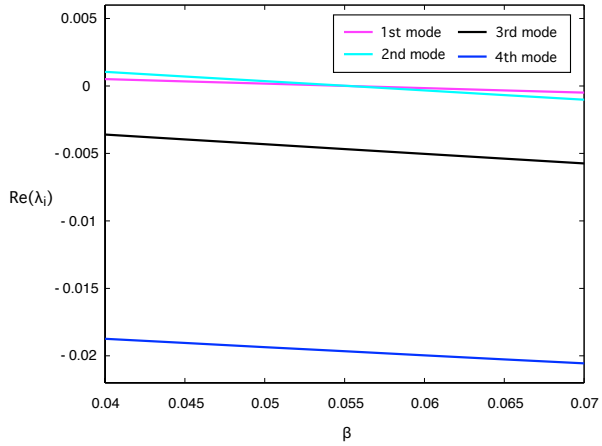

Fig. 4.7: Plotted is the real part of the complex frequencies $\mathrm{Re}\,\lambda_j$ for the first four modes $j = 1, 2, 3, 4$ as a function of the feedback parameter β in the vicinity of the critical point $(\alpha, \beta) = (2.176, 0.055)$, with $\delta = 0.55$, where the two modes $j = 1, 2$ lose their stability simultaneously.

Writing the functions $q_n(t)$ and $h_n(t)$ with $n = 1, \ldots, N$ as the Fourier series

$$\begin{pmatrix} q_n(t) \\ h_n(t) \end{pmatrix} = \sum_{j=-\frac{N}{2}+1}^{\frac{N}{2}} \begin{pmatrix} Q_j(t) \\ H_j(t) \end{pmatrix} \exp\left(\frac{2\pi i j n}{N}\right),$$

the system (4.16) becomes

$$\delta\ddot{Q}_j + \dot{Q}_j + \delta\ddot{H}_j + \dot{H}_j = \gamma_j \left(Q_j - \frac{1}{3} \sum_{j_1, j_2, j_3} Q_{j_1} Q_{j_2} Q_{j_3} \delta_{j, j_1+j_2+j_3} \right) \tag{4.17}$$

$$(\alpha + \beta)\dot{H}_j + H_j + \beta\dot{Q}_j = 0, \tag{4.18}$$

where $\delta_{k,l}$ denotes the Kronecker delta function and

$$\gamma_j = e^{2\pi i j/N} - 1.$$

Note that the equation for $j = 0$ reduces to

$$\delta\ddot{Q}_0 + \dot{Q}_0 = -\delta\ddot{H}_0 - \dot{H}_0, \qquad (\alpha + \beta)\dot{H}_0 + H_0 = -\beta\dot{Q}_0.$$

We will set $(Q_0, H_0) \equiv 0$ in the following. Since (q_n, h_n) are real-valued, the Fourier amplitudes (Q_j, H_j) satisfy the identity $(Q_{-j}, H_{-j}) = (\overline{Q_j}, \overline{H_j})$, and we can therefore focus on the equations for $j > 0$.

We now choose parameter values (α, β, τ) such that the modes $j = 1, 2$ are linearly unstable, whilst the modes with $j > 2$ are linearly stable: see Figure 4.7 for an example

of such parameter values, which correspond to the case plotted in Figure 4.4(1). To obtain a reduced model, we will include the equation for the mode $j = 3$ but set all other modes to zero. Thus, the equations (4.17) for Q_j with $j = 1, 2, 3$ become

$$\begin{aligned}
\delta\ddot{Q}_1 + \dot{Q}_1 + \delta\ddot{H}_1 + \dot{H}_1 &= \gamma_1 \left[(1 - |Q_1|^2 - 2|Q_2|^2 - 2|Q_3|^2)Q_1 - \overline{Q_1}^2 Q_3 - Q_2^2\overline{Q_3}\right] \\
\delta\ddot{Q}_2 + \dot{Q}_2 + \delta\ddot{H}_2 + \dot{H}_2 &= \gamma_2 \left[(1 - 2|Q_1|^2 - |Q_2|^2 - 2|Q_3|^2)Q_2 - 2Q_1\overline{Q_2}Q_3\right] \\
\delta\ddot{Q}_3 + \dot{Q}_3 + \delta\ddot{H}_3 + \dot{H}_3 &= \gamma_3 \left[(1 - 2|Q_2|^2 - 2|Q_1|^2 - |Q_3|^2)Q_3 - \frac{1}{3}Q_1^3 - \overline{Q_1}Q_2^2\right],
\end{aligned} \tag{4.19}$$

while equation (4.18) for H_j, given by

$$(\alpha + \beta)\dot{H}_j + H_j + \beta\dot{Q}_j = 0, \qquad j = 1, 2, 3, \tag{4.20}$$

remains unchanged. The free-flow solution corresponds to the equilibrium $(Q, H) = 0$ of (4.19)-(4.20). We seek traffic-jam solutions of (4.19)-(4.20) as rotating waves, which are of the form

$$Q_j(t) = A_j e^{i(j\omega t + \varphi_j^A)}, \qquad H_j(t) = B_j e^{i(j\omega t + \varphi_j^B)}, \tag{4.21}$$

where the amplitudes (A_j, B_j), the phases $\varphi_j^{A,B}$, and the frequency ω are real constants. Note that 1-jam solutions correspond to $(A_2, B_2) = 0$, while 2-jam solutions have $(A_1, B_1) = (A_3, B_3) = 0$.

Existence of 2-jam solutions. First, we consider 2-jam solutions. Setting $(Q_1, Q_3, H_1, H_3) = 0$ and substituting the ansatz (4.21) for $j = 2$ into (4.19)-(4.20), we find that ω is determined by the equation

$$\frac{2\omega\left(4\alpha\delta\omega^2(\alpha + \beta) - \beta + \delta\right)}{4\omega^2(\alpha(\alpha + \beta) + \beta\delta) + 1} - \tan\left(\frac{2\pi}{N}\right) = 0, \tag{4.22}$$

while the amplitudes (A_2, B_2) and the phase difference $\varphi_2^A - \varphi_2^B$ are given by

$$\begin{aligned}
B_2 &= -\frac{2i\alpha\omega}{1 + 2i(\alpha + \beta)\omega} A_2 e^{i(\varphi_2^A - \varphi_2^B)} \\
A_2^2 &= 1 - \omega \csc\left(\frac{2\pi}{N}\right) \sqrt{\frac{(4\alpha^2\omega^2 + 1)\,(4\delta^2\omega^2 + 1)}{4\alpha^2\omega^2 + 8\alpha\beta\omega^2 + 4\beta^2\omega^2 + 1}}.
\end{aligned}$$

To investigate the stability of the 2-jam solutions, we seek perturbed solutions in the form

$$Q_j(t) = \left(A_j + \xi_j e^{zt}\right) e^{i\varphi_j^A} e^{ij\omega t}, \qquad H_j(t) = \left(B_j e^{i\varphi_j^B} + \eta_j e^{\lambda t + i\varphi_j^A}\right) e^{ij\omega t}, \tag{4.23}$$

where ξ_j and η_j are complex amplitudes, and λ is a complex growth rate. Substituting this expression into (4.19)-(4.20) and linearizing in (ξ_j, η_j) about zero, we arrive at a

linear system for the amplitude (ξ_j, η_j), which has a nontrivial solution if, and only if, the growth rate λ satisfies

$$Z_1\overline{Z_3} - A_2^4 = 0, \qquad Z_2\overline{Z_2} - A_2^4 = 0, \tag{4.24}$$

where

$$Z_j = -\left(1 - 2A_2^2\right) + \frac{f(\lambda + ij\omega)}{\gamma_j}, \qquad f(x) = \frac{x(1+\alpha x)(1+\delta x)}{1 + (\alpha+\beta)x}. \tag{4.25}$$

We can solve equation(4.22) for the frequency ω and the system (4.24) for the stability numerically and will present the results below.

Existence of 1-jam solutions. Next, we consider the existence and stability of 1-jam solutions. Setting $(Q_2, H_2) = 0$ and substituting the expression (4.21) for $j = 1, 2$ into (4.19)-(4.20), we find that the amplitudes (A_1, A_3), the phase difference $\Delta = \varphi_3^A - 3\varphi_1^A$, and the frequency ω are determined by the equations

$$\left[f(i\omega) - \gamma_1(1 - A_1^2 - 2A_3^2)\right] = -\gamma_1 A_3 A_1 e^{i\Delta}, \qquad \left[f(3i\omega) - \gamma_3(1 - 2A_1^2 - A_3^2)\right] A_3 = -\frac{1}{3}\gamma_3 A_1^3 e^{-i\Delta}. \tag{4.26}$$

To determine the stability of the 1-jam solutions, we again substitute the ansatz (4.23) into (4.19)-(4.20). Linearizing in (ξ_j, η_j) about zero results in the characteristic equation $\det \mathcal{L}(\lambda) = 0$ for the modes $j = 1, 3$ and the equation

$$G_2\overline{G_2} - 4A_1^2A_3^2 = 0$$

for $j = 2$, where

$$\mathcal{L}(\lambda) = \begin{pmatrix} G_1 & 2A_3A_1e^{i\Delta} + A_1^2 & {A_1}^2e^{-i\Delta} + 2A_1A_3 & 2A_1A_3 \\ A_1^2 + 2A_1A_3e^{-i\Delta} & G_{-1} & 2A_1A_3 & 2A_3A_1 + A_1^2e^{i\Delta} \\ 2A_3A_1 + A_1^2e^{i\Delta} & 2A_1A_3 & G_3 & A_3^2 \\ 2A_1A_3 & A_1^2e^{-i\Delta} + 2A_1A_3 & A_3^2 & G_{-3} \end{pmatrix}$$

and

$$G_j = 2(A_1^2 + A_3^2) + \frac{f(\lambda + ij\omega)}{\gamma_j} - 1.$$

Evaluating the existence and stability conditions numerically, we arrive at the bifurcation diagram in the (α, β) parameter space plotted in Figure 4.8.

4.4. Modulated waves. We now present the results of numerical computations of the bifurcating modulated waves that bifurcate from k-jam solutions. As mentioned earlier, modulated waves are of the form

$$(d_n, v_n, h_n)(t) = (d_*(n - ct, \omega t), v_*(n - ct, \omega t), h_*(n - ct, \omega t)) \tag{4.27}$$

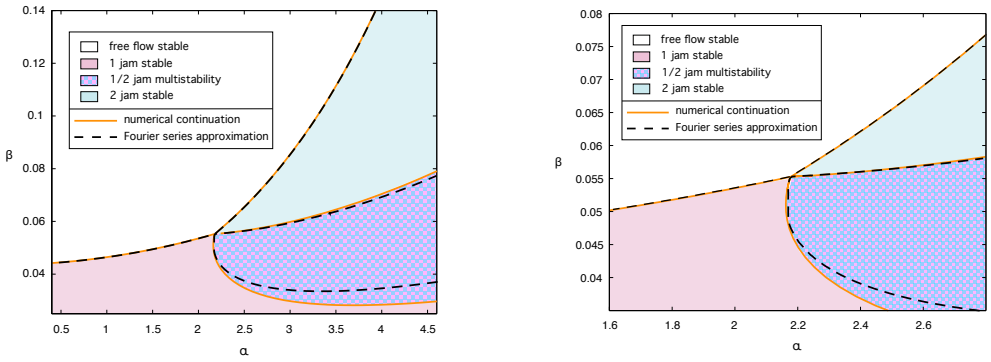

Fig. 4.8: Plotted is a comparison of the bifurcation diagrams obtained from the reduced three-dimensional Fourier-series approximation and the numerical continuation for $N = 30$, and $L = 30$ with $\delta = 0.55$. The right panel is a magnification of the left panel near the bifurcation point.

where $(d_*, v_*, h_*)(x, \tau)$ is N-periodic in x and 2π-periodic in τ. Here (c, ω) depend on (α, β) with ω being close to the imaginary part of the Hopf eigenvalue of the k-jam solution near onset. In particular, these modulated waves can be found as solutions to the following planar boundary-value problem. Using the above ansatz, we arrive at the system

$$\begin{aligned} \omega d_\tau - c d_x &= v(x,\tau) \qquad (4.28)\\ \delta\left(\omega v_\tau - c v_x\right) &= \tanh(d(x+1,\tau) - h(x+1,\tau)) - \tanh(d(x,\tau) - h(x,\tau)) - v(x,\tau)\\ \alpha\left(\omega h_\tau - c h_x\right) &= -h(x,\tau) - \beta v(x,\tau). \end{aligned}$$

These equations are supplemented with the boundary conditions

$$\begin{aligned} d(x+N,\tau) &= d(x,\tau) \qquad h(x+N,\tau) = h(x,\tau) \qquad (4.29)\\ d(x,\tau+2\pi) &= d(x,\tau) \qquad h(x,\tau+2\pi) = h(x,\tau) \qquad \forall x,\tau, \end{aligned}$$

and the constraint

$$\sum_{n=1}^{N} d(n,\tau) = 0 \quad \forall \tau. \qquad (4.30)$$

We used branch switching and numerical continuation in Matlab to compute the modulated rotating waves that bifurcate in the parameter region depicted in Figure 4.4(1). As can be seen from this figure, we can keep α constant and vary the parameter β to move from the region of 1-jam stability to the region of 2-jam stability. Starting from a stable 1-jam solution, branch switching was used at the 2-jam stability boundary to find the modulated-wave solution which was then continued in β through the

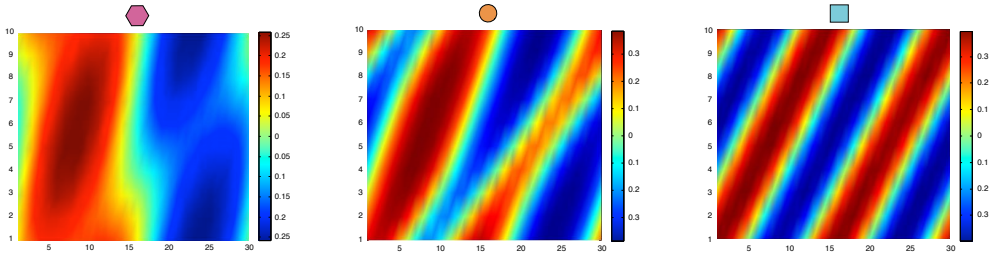

(a) solution near the 2-jam stability boundary

(b) solution in the middle of the 1-jam/2-jam multi-stability region

(c) solution near the 1-jam stability boundary

Fig. 4.9: Shown are space-time color plots of the distances (space is horizontal, and time vertical) for modulated-wave solutions in the multi-stability region of 1- and 2-jam solutions with $N = 30$. The labels above each panel refer to the respective location along the continuation curve shown in Figure 4.4(1).

region of multi-stability to the 1-jam stability boundary. This is represented by the arrowed line shown in Figure 4.4(1). Figure 4.9 depicts the progression of this solution throughout the continuation scheme.

A similar method was used in the region depicted in Figure 4.4(2) to find the modulated-wave solution that exists in the region of multi-stability between the 2-jam and 3-jam stability curves. Figure 4.10 shows the time periodic solution which connects the 2-jam and 3-jam solutions in this region. We expect that similar solutions exist in the other regions of multi-stability.

5. Fundamental diagrams and energy consumption. In this section, we present the fundamental diagrams that relate flux and density in traffic flows and calculate the energy consumption of free-flow and traffic-jam solutions. The flux of cars is among the most important quantities that characterize traffic dynamics. Using the microscopic flux ([10], [17])

$$J(x,t) = \sum_n \dot{p}_n(t)\delta\left(x - p_n(t)\right) \tag{5.1}$$

and the microscopic density

$$\rho(x,t) = \sum_n \delta\left(x - p_n(t)\right), \tag{5.2}$$

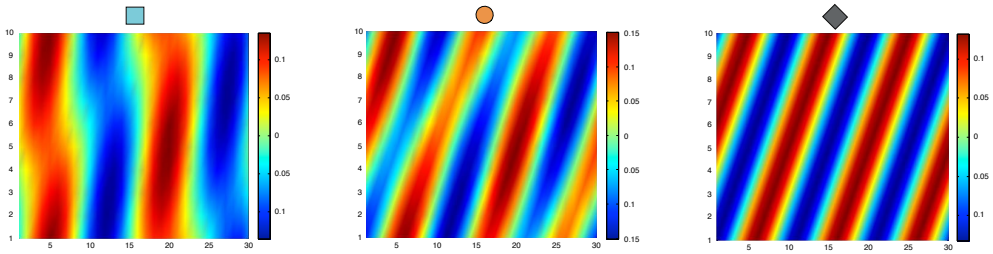

(a) solution near the 3-jam stability boundary

(b) solution in the middle of the 2-jam/3-jam multi-stability region

(c) solution near the 2-jam stability boundary

Fig. 4.10: Shown are space-time color plots of the distances (space is horizontal, and time vertical) for modulated-wave solutions in the multi-stability region of 2- and 3-jam solutions with $N = 30$. The labels above each panel refer to the respective location along the continuation curve shown in Figure 4.4(2).

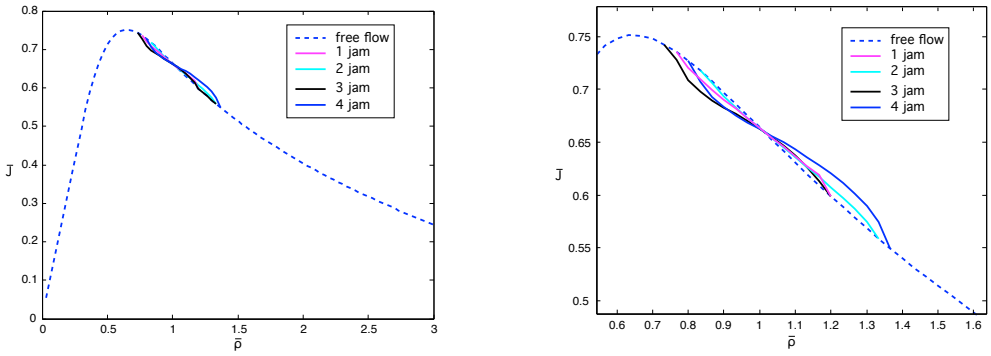

(a) Fundamental diagram.

(b) Zoom of fundamental diagram.

Fig. 5.1: Shown are the fundamental diagrams for the free flow, 1-jam, 2-jam, 3-jam, and 4-jam solutions: plotted is the flux $\bar{J}$ as a function of the density $\bar{\rho}$. The 1-jam and 2-jam solutions were obtained for $(\alpha, \beta) = (2.2, 0.01)$, and the 3-jam and 4-jam solutions were obtained for $(\alpha, \beta) = (4, 2.4)$. Note that the flux for the free flow is independent of the parameters α and β.

we see that the continuity equation $\rho_t + J_x = 0$ holds formally. The mean flux is given by the expression

$$\bar{J}(t) = \frac{1}{L} \int_0^L J(x,t)dx = \bar{\rho}\bar{U}(t), \tag{5.3}$$

where

$$\bar{U}(t) = \frac{1}{N} \sum_n \dot{p}_n(t) \tag{5.4}$$

is the mean velocity, and $\bar{\rho} = N/L$ is the mean density of cars. We choose the value $v_0 = \tanh(0.8)$ in (1.2) and compute the fundamental diagrams by plotting the mean flux $\bar{J}(t)$ averaged over one period as a function of the density $\bar{\rho}$. The fundamental diagrams for the free-flow solution and for k-jam solutions with $k = 1, 2, 3, 4$ at different values of (α, β) are shown in Figure 5.1. Thus, upon varying (α, β), the k-jam solutions seem to fill out an open area in density-flux space.

Reproducing fundamental diagrams of real traffic flows, and in particular their multivalued nature, is one of the goals of traffic-flow modeling. In the recent work [22], fundamental diagrams were generated from real sensor measurement data that were aggregated over 30-second intervals and successfully compared with those obtained from the traveling waves of a macroscopic traffic-flow model; see Figure 5.2a. Since we can view (α, β) as characteristics of individual drivers, we proceed similarly by running direct numerical simulations with the amended optimal velocity model (1.2): a solution is generated and evolved forward for a fixed duration during which the number of cars passing through a certain fixed location is counted, thus emulating a physical sensor on a highway. This procedure is repeated for values of (α, β) with $2 \leq \alpha \leq 4$ and $0.02 \leq \beta \leq 4.02$, which yields the diagram shown in Figure 5.2b, where the data points have been superimposed on the free flow curve. Thus, while a full study of the effect of the traveling-wave solutions found in this paper on the fundamental diagram and the comparison with traffic data is beyond the scope of this paper, the simulations in Figure 5.2b show promise for explaining traffic data using the model (1.2) when varying the model parameters.

Vehicle flux characterizes the efficiency of traffic flow, and it is therefore natural to ask how much energy is consumed in such a flow. To address this question for the flows observed in our model, we use the vehicle-specific power approach to emissions characterization [20]. Using the formula and coefficients in [20, Equation (2)], we can write the average vehicle-specific power as

$$C(t) = \frac{1}{N} \sum_{n=1}^{N} \left[1.04 \left(\frac{1}{2} \frac{d}{dt} \dot{p}_n^2(t) \right) H(\ddot{p}_n(t)) + 0.132\, \dot{p}_n(t) + 0.0021\, \dot{p}_n(t)^3 \right], \tag{5.5}$$

where $H(x)$ is the Heaviside step function. The first term in this expression represents the rate at which the kinetic energy of each car changes under acceleration, the second term represents the resistance to rolling, and the final term represents aerodynamic resistance; in comparison with the formula in [20], we have assumed that the road

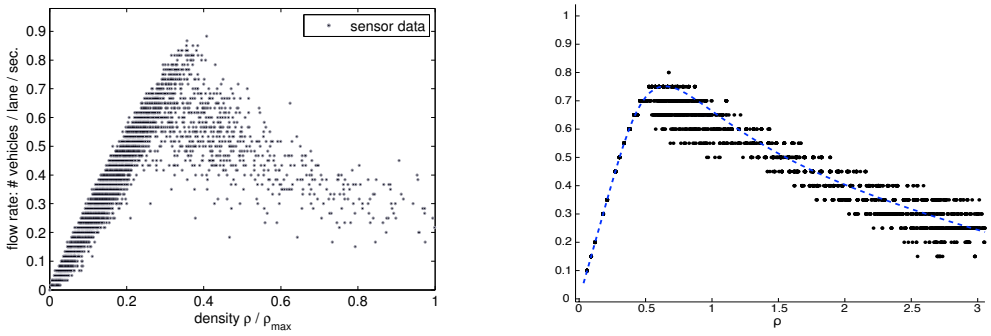

(a) Real traffic data [22].

(b) Numerical simulations.

Fig. 5.2: Comparison of fundamental diagrams obtained from real traffic data, reproduced with permission from [22], and the extended model (1.2).

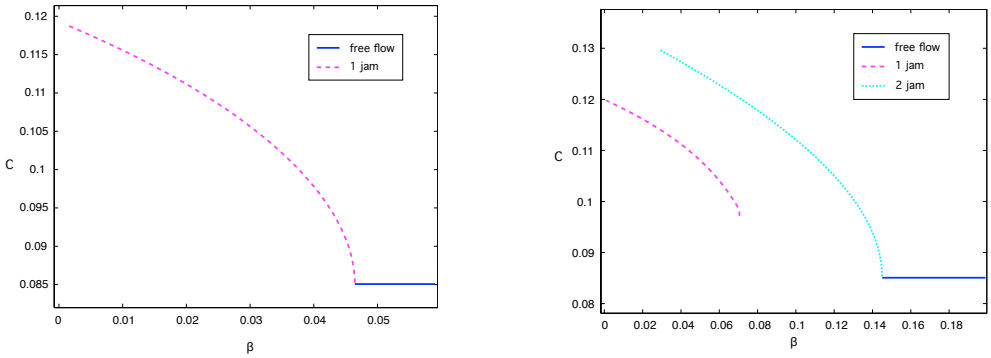

(a) $\alpha = 1$

(b) $\alpha = 4$

Fig. 5.3: Shown is the average fuel consumption C as a function of the parameter β for free flow and k-jam solutions in their respective regions of stability.

grade is zero. Figure 5.3 shows the fuel consumption as a function of β for the free flow, 1-jam and 2-jam solutions for two different values of α: plotted is the average value of $C(t)$ over one period as a function of β.

6. Discussion. In this paper, we studied the traffic flow of a fixed number of cars on a ring road under an optimal-velocity model augmented with an equation for the individual target headways. We focussed primarily on the case when $\ell = 0$, i.e. when the optimal headway $\bar{s}$ coincides with the average distance L/N between cars. We looked at the dependence of the flow on the model parameters α and β that represent the adjustment time and a measure of the proactiveness of drivers,

respectively. We found that the model admits a free-flow solution which is stable in a bounded region in the (α, β) space. The boundary of this region was computed numerically and is composed of curves representing supercritical Hopf bifurcations to rotating-wave solutions that correspond to traffic jams. The stability boundaries of the traffic-jam solutions were also computed numerically and were found to originate from codimension-two bifurcation points at which the free-flow solution undergoes a double Hopf bifurcation in two different wave numbers. Near these points, normal-form analysis was used to confirm the numerical results. The resulting bifurcation diagram is shown in Figure 4.5 and indicates that stable traffic-jam solutions can coexist; their basins are separated by the stable manifolds of unstable modulated-wave solutions that we computed numerically. We note that, while traffic-jam solutions can coexist, we did not find regions in which free-flow and traffic-jam solutions coexist.

Our model allows for drivers to reduce or increase their target headways if the velocity difference to the car ahead increases or decreases. The parameter β describes how much a driver reacts to the velocity of the car ahead. We found that high β values result in traffic jams, indicating that drivers who react too strongly to changes in traffic flow may cause jams. However, very low β values also result in traffic jams, so to avoid jams, fluctuations in distances between adjacent cars should elicit a moderate reaction from the drivers. In addition, we note that higher values of α also result in traffic jam solutions, which suggests that slower reaction times also cause jams; this is analogous to the effect of the parameter δ in the original optimal velocity model. An interesting extension would be to consider stochastic variations in the parameters (α, β) to simulate groups of drivers with different driving strategies: it is not clear what the impact of such variations on the occurrence of traffic jams and on fundamental diagrams would be.

The k-jam solutions found in this paper arise intrinsically and without external triggers in our model. Even though multi-jam solutions have not yet been observed in closed ring-road scenarios, traffic data from the German highway A5 indicates the existence of such multi-jams in systems with exits and entrances [26, 27]. It is possible that the multi-jams observed on the A5 arise intrinsically even without exit and entrance ramps, but only a controlled experiment such as the one for single jams presented in [23, 24] could answer this question. We remark that experimental studies of pedestrian traffic on ring roads exhibit multi-jams (see [16, Figure 1]).

We recall that the parameter $\ell = L/N - \bar{s}$ represents the mismatch between the optimal headway and the average distance of the cars on the road and therefore the overall traffic density. We did not carry out a systematic study of the effect of ℓ on the underlying traffic-flow dynamics: a more systematic study could be performed

and could perhaps shed light on a variety of different driving scenarios.

An interesting question from a modeling perspective is whether the microscopic model considered here can yield a macroscopic model via an appropriate continuum limit, similar to the results in [1]. We believe that a limiting macroscopic model exists but have not studied this question in detail.

Acknowledgments. The authors are grateful to the referees for constructive comments that helped improve the conclusions of this paper. Gaididei acknowledges partial financial support from the Ukrainian National Academy of Sciences and a Guest Professorship funded by grants from the Civilingeniør Frederik Christiansens Almennyttige Fond, the IKERBASQUE Foundation (Bilbao, Spain), and the Danish Centre for Applied Mathematics and Mechanics (DCAMM). Sandstede was partially supported by the NSF under grant DMS-0931908.

References.

[1] A Aw, A Klar, M Rascle, and T Materne, *Derivation of continuum traffic flow models from microscopic follow-the-leader models*, SIAM J. Appl. Math., 63 (2002), pp. 259–278.

[2] A Aw and Michel Rascle, *Resurrection of" second order" models of traffic flow*, SIAM J. Appl. Math., 60 (2000), pp. 916–938.

[3] Masako Bando, Katsuya Hasebe, Akihiro Nakayama, Akihiro Shibata, and Yuki Sugiyama, *Dynamical model of traffic congestion and numerical simulation*, Phys. Rev. E, 51 (1995), pp. 1035–1042.

[4] M. Beck, Hermen Jan Hupkes, Björn Sandstede, and Kevin Zumbrun, *Nonlinear stability of semidiscrete shocks for two-sided schemes*, SIAM J. Math. Anal., 42 (2010), pp. 857–903.

[5] Nicola Bellomo and Christian Dogbe, *On the modeling of traffic and crowds: A survey of models, speculations, and perspectives*, SIAM Rev., 53 (2011), pp. 409–463.

[6] M Flynn, A Kasimov, J-C Nave, R Rosales, and B Seibold, *Self-sustained nonlinear waves in traffic flow*, Phys. Rev. E, 79 (2009), p. 056113.

[7] Yuri Gaididei, Rainer Berkemer, Carlos Gorria, Peter L. Christiansen, Atsushi Kawamoto, Takahiro Shiga, Mads P. Sørensen, and Jens Starke, *Complex spatiotemporal behavior in a chain of one-way nonlinearly coupled elements*, Discr. Cont. Dynam. Syst. S, 4 (2011), pp. 1167–1179.

[8] Yu. B. Gaididei, R. Berkemer, J. G. Caputo, P. L. Christiansen, A. Kawamoto, T. Shiga, M. P. Sørensen, and J. Starke, *Analytical solutions of jam pattern formation on a ring for a class of optimal velocity traffic models*, New J. Phys., 11 (2009), pp. 073012, 19 pp.

[9] Yuri B. Gaididei, Carlos Gorria, Rainer Berkemer, Peter L. Christiansen, Atsushi Kawamoto, Mads. P. Sørensen, and Jens Starke, *Stochastic control of traffic patterns*, Networks & Heterogen. Media, 8 (2013), pp. 261–273.

[10] Y. B. Gaididei, C. Gorria, R. Berkemer, A. Kawamoto, T. Shiga, P. L. Christiansen, M. P. Sørensen, and J. Starke, *Controlling traffic jams by time-modulating the safety distance*, Phys. Rev. E, (2013).

[11] Martin Golubitsky and D Schaeffer, *Singularities and Groups in Bifurcation Theory II*, Springer-Verlag, 1988.

[12] J M Greenberg, *Congestion redux*, SIAM J. Appl. Math., 64 (2004), pp. 1175–1185.

[13] John Guckenheimer and Philip Holmes, *Nonlinear oscillations, dynamical systems, and bifurcations of vector fields*, vol. 42, Springer-Verlag New York, 1983.

[14] M Gunther, A Klar, T Materne, and R Wegener, *An explicitly solvable kinetic model for vehicular traffic and associated macroscopic equations*, Math. Comp. Model., 35 (2002), pp. 591–606.

[15] Dirk Helbing, *Traffic and related self-driven many-particle systems*, Rev. Mod. Phys., 73 (2001), p. 1067.

[16] Asja Jelić, Cécile Appert-Rolland, Samuel Lemercier, and Julien Pettré, *Properties of pedestrians walking in line: Fundamental diagrams*, Phys. Rev. E, 85 (2012), p. 036111.

[17] HK Lee, H-W Lee, and D Kim, *Macroscopic traffic models from microscopic car-following models*, Physical Review E, 64 (2001), p. 056126.

[18] Takashi Nagatani, *The physics of traffic jams*, Rep. Progr. Phys., 65 (2002), p. 1331.

[19] K NAGEL and M SCHRECKENBERG, *A cellular automaton model for freeway traffic*, J. Phys. I, 2 (1992), pp. 2221–2229.

[20] Edward K Nam, *Proof of concept investigation for the physical emission rate estimator (pere) to be used in moves*, Assessment and Standards Division Office of Transportation and Air Quality, US EPA., (2003).

[21] Bjorn Sandstede and Arnd Scheel, *Essential instabilities of fronts: bifurcation, and bifurcation failure*, Dynam. Syst., 16 (2001), pp. 1–28.

[22] Benjamin Seibold, Morris R Flynn, Aslan R Kasimov, and Rodolfo Ruben Rosales, *Constructing set-valued fundamental diagrams from jamiton solutions in second order traffic models.*, Networks & Heterog. Media, 8 (2013).

[23] Yuki Sugiyama, Minoru Fukui, Macoto Kikuchi, Katsuya Hasebe, Akihiro Nakayama, Katsuhiro Nishinari, Shin-Ichi Tadaki, and Satoshi Yukawa, *Traffic jams without bottlenecks—experimental evidence for the physical mechanism of the formation of a jam*, New J. Phys., 10 (2008), p. 033001.

[24] Shin-Ichi Tadaki, Macoto Kikuchi, Minoru Fukui, Akihiro Nakayama, Katsuhiro Nishinari, Akihiro Shibata, Yuki Sugiyama, Taturu Yosida, and Satoshi Yukawa, *Phase transition in traffic jam experiment on a circuit*, New J. Phys., 15 (2013), p. 103034.

[25] Floris Takens, *Singularities of vector fields*, Publ. Math. l'IHÉS, 43 (1974), pp. 47–100.

[26] M. Treiber and A. Kesting. `http://www.traffic-states.com`, 2013.

[27] M. Treiber, A. Kesting, and R. E. Wilson, *Reconstructing the traffic state by fusion of heterogeneous data*, Computer-Aided Civil Infra. Eng., 26 (2011), pp. 408–419.

[28] DE Wolf, M Schreckenberg, and A Bachem, *Traffic and granular flow*, World Scientific, Singapore, 1996.